

Ferroelectric Properties of Aurivillius Phase $\text{Bi}_5\text{Cr}_x\text{Fe}_{1-x}\text{Ti}_3\text{O}_{15}$ Films

by

Junyan Zhang

Bachelor of Engineering, Shandong University, 2018

Submitted to the Graduate Faculty of the
Swanson School of Engineering in partial fulfillment
of the requirements for the degree of
Master of Science in Materials Science and Engineering

University of Pittsburgh

2020

UNIVERSITY OF PITTSBURGH
SWANSON SCHOOL OF ENGINEERING

This thesis was presented

by

Junyan Zhang

It was defended on

March 25, 2020

and approved by

Ian Nettleship, Ph.D., Associate Professor, Department of Mechanical Engineering and Materials
Science

Paul Ohodnicki, Ph.D., Associate Professor, Department of Mechanical Engineering and
Materials Science

Thesis Advisor: Jung-Kun Lee, Ph.D., Professor, Department of Mechanical Engineering and
Materials Science

Copyright © by Junyan Zhang

2020

Ferroelectric Properties of Aurivillius Phase $\text{Bi}_5\text{Cr}_x\text{Fe}_{1-x}\text{Ti}_3\text{O}_{15}$ Films

Junyan Zhang, MS

University of Pittsburgh, 2020

Aurivillius phase $\text{Bi}_5\text{Cr}_x\text{Fe}_{1-x}\text{Ti}_3\text{O}_{15}$ ($\text{BC}_x\text{F}_{1-x}\text{TO}$) thin films are prepared by the chemical solution deposition method and the effect of Cr content on the structural, optical bandgap, electric transport, and dielectric/ferroelectric properties of $\text{BC}_x\text{F}_{1-x}\text{TO}$ thin films are investigated in detail. X-ray diffraction analysis shows that all of $\text{BC}_x\text{F}_{1-x}\text{TO}$ films are a complete solid solution and maintain Aurivillius structure. The replacement of Fe^{3+} with smaller Cr^{3+} decreases the overall lattice volume and gradually increases the bandgap of $\text{BC}_x\text{F}_{1-x}\text{TO}$ thin film. The random mixing of Cr and Fe in $\text{BC}_x\text{F}_{1-x}\text{TO}$ decreases the long-range lattice distortion in a-b plane and the smallest a/b ratio is found at $\text{BC}_{0.5}\text{F}_{0.5}\text{TO}$. Cr-doping also changes the grain shape from the spheres to plates and $\text{BC}_{0.5}\text{F}_{0.5}\text{TO}$ consists of only plate-like grains. This indicates that a decrease in the lattice distortion promotes the grain growth along a-b plane and facilitates the appearance of the inherent crystal shape of Aurivillius phase. Ferroelectric properties of $\text{BC}_x\text{F}_{1-x}\text{TO}$ films are examined by measuring P-E hysteresis loops. Cr-doping increases saturated polarization (P_s) and decreases coercive field (E_c). When 50 atomic % of Cr is doped, P_s and E_c of $\text{BC}_{0.5}\text{F}_{0.5}\text{TO}$ is $35 \mu\text{C}/\text{cm}^2$ and $125 \text{ kV}/\text{cm}$, respectively. This is due to the fact that the decrease in the long-range distortion in a-b plane promotes the alignment of ferroelectric dipoles under electric field. The frequency

dependent dielectric properties at different temperatures and the leakage current show that Cr doping increases the carrier concentration and the space charge polarization. However, the plate-like shape grains of Cr-rich $\text{BC}_x\text{F}_{1-x}\text{TO}$ films suppress the transport of carriers from grains to grains and prevents a dramatic increase in the leakage current. The results of this study provide a design rule to control the ferroelectric of Aurivillius phase $\text{BC}_x\text{F}_{1-x}\text{TO}$ thin films by modifying the composition and lattice distortion.

Table of Contents

Nomenclature	xiii
1.0 Introduction.....	1
2.0 Background Information and Literature Review	3
2.1 Ferroelectric Materials	3
2.1.1 Ferroelectric Materials Development History	3
2.1.2 Applications of Ferroelectric Materials	5
2.1.3 Multiferroic Materials	6
2.1.4 Aurivillius Phase Materials	7
2.1.5 Bi ₅ FeTi ₃ O ₁₅ and Thin Film Ferroelectric Materials	9
2.2 Ferroelectric and Dielectric Properties	11
2.2.1 Spontaneous Polarization in Ferroelectrics	11
2.2.2 Ferroelectric Domains and P-E Hysteresis Loop	13
2.2.3 Dielectric Constant and Loss Factor	14
2.2.4 Leakage Current in Ferroelectric Thin Films	16
2.3 Doping Effect in Ferroelectrics	16
2.3.1 A Change in Multiferroic Property by Impurity Doping.....	16

2.3.2 A Change in Multiferroic Property of Aurivillius Phases by Impurity Doping	17
2.3.3 Cr-doping Effect	18
3.0 Research Description	19
3.1 Hypothesis	19
3.2 Objectives	19
3.3 Tasks	19
4.0 Experiment Details	21
4.1 Precursor Preparation	21
4.2 Coating and Annealing Procedure	21
4.3 Electrode Deposition	22
4.4 Crystal Structure and Bandgap	23
4.4.1 X-ray Diffraction Test	23
4.4.2 Ultraviolet-visible Spectroscopy Test	23
4.5 Microstructure and Ferroelectric Property	23
4.5.1 Scanning Electron Microscope Test	23
4.5.2 Ferroelectric Property Measurement	23
4.6 Dielectric Property and Leakage Current Density	24

4.6.1 Dielectric Property Measurement.....	24
4.6.2 Leakage Current Measurement.....	24
5.0 Result and Discussion	25
5.1 Crystal Structure and Bandgap (Composition Effect)	25
5.2 Microstructure and Ferroelectric Property (Shape Effect)	29
5.3 Dielectric Property and Leakage Current Density (Leakage Behavior).....	37
6.0 Conclusion	50
Bibliography	51

List of Tables

Table 1 The Conduction Mechanisms of BFTO and BCTO Films under Different Electric Field.....	49
---	-----------

List of Figures

Figure 1. Interrelationship Among Piezoelectric, Ferroelectric, Pyroelectric, and Dielectric Materials	6
Figure 2. Prototype of the Aurivillius Structure as a Function of the Number of Pseudo-perovskite Layers	8
Figure 3. Spontaneous Polarization Model.....	11
Figure 4. The Normal Relationship Between Polarization and Temperature.	12
Figure 5. The Classic Hysteresis Loop	14
Figure 6. The Procedure of Ferroelectric Thin Films' Preparation.....	22
Figure 7. (a) XRD Patterns, Plotted as Log Intensity Versus 2θ, of the Substrate and the $\text{Bi}_5\text{Cr}_x\text{Fe}_{1-x}\text{Ti}_3\text{O}_{15}$ Thin Films for $x=0, 0.1, 0.3, 0.5,$ and 1 from the Bottom Up (b) A Change in the Lattice Parameter of C-axis With Different Cr-doping Content	26
Figure 8. (a) Local Broadened XRD Pattern of 2θ Around the Diffraction Peak Located at (200/020) (b) The Variation of the Lattice Parameters $a, b,$ and Lattice Distortion a/b of Samples with Cr-doping Content.....	27
Figure 9. (a) The Ultraviolet-visible Transmittance Spectra for $\text{Bi}_5\text{Cr}_x\text{Fe}_{1-x}\text{Ti}_3\text{O}_{15}$ Films (b) The Plot of $(\alpha h\nu)^2$ as a Function of Photon Energy Around the Absorption Edge	29

Figure 10. The SEM Images of the $\text{Bi}_5\text{Cr}_x\text{Fe}_{1-x}\text{Ti}_3\text{O}_{15}$ Thin Films for: (a) $x=0$, (b) $x=0.1$, (c) $x=0.3$, (d) $x=0.5$, (e) $x=1$	31
Figure 11. P-E Hysteresis Loops of the $\text{Bi}_5\text{Cr}_x\text{Fe}_{1-x}\text{Ti}_3\text{O}_{15}$ Thin Films at a Measurement Frequency of 100 Hz for: (a) $x=0$, (b) $x=0.1$, (c) $x=0.3$, (d) $x=0.5$, (e) $x=1$.....	32
Figure 12. The Variation of the Saturation Polarization, Remnant Polarization and Coercive Field as a Function of Cr-doping Content.....	34
Figure 13. P-E Hysteresis Loops at Different Voltages with the Frequency of 100 Hz of the Pure BFTO Thin Film	36
Figure 14. The Frequency Dependences of: (a) Dielectric Constant ϵ_r (b) Loss Tangent $\tan\delta$ for all these BCFTO Samples	37
Figure 15. The Variation of the ϵ_r and $\tan\delta$ of Samples at 1kHz with Cr-doping Content .	39
Figure 16. The Frequency Dependency of ϵ_r of the BCFTO Thin Films at Various Temperatures for: (a) $x=0$, (b) $x=0.1$, (c) $x=0.3$, (d) $x=0.5$, (e) $x=1$	42
Figure 17. The Frequency Dependency of $\tan\delta$ of the BCFTO Thin Films at Various Temperatures for: (a) $x=0$, (b) $x=0.1$, (c) $x=0.3$, (d) $x=0.5$, (e) $x=1$	43
Figure 18. The Electric Field Dependence of Leakage Current Density (J-E) of All BCFTO Samples	44

Figure 19. Various Fits of J-E Curves Using Different Leakage Current Mechanisms: (a) PF Emission: $\ln(J/E)$ Versus $E_{1/2}$ Curves, (b) FN Tunneling: $\ln(J/E^2)$ Versus $1/E$ Curves, (c) Schottky Emission: $\ln J$ Versus $E_{1/2}$ Curves, (d) Ohmic and SCLC: $\ln J$ Versus $\ln E$ Curves..... 46

Nomenclature

Aurivillius structure	$(\text{Bi}_2\text{O}_2)_{2+}(\text{A}_{n-1}\text{B}_n\text{O}_{3n+1})_{2-}$
BCFTO	$\text{Bi}_5\text{Cr}_x\text{Fe}_{1-x}\text{Ti}_3\text{O}_{15}$
Rochelle salt	$\text{NaKC}_4\text{H}_4\text{O}_6 \cdot 4\text{H}_2\text{O}$
KDP	KH_2PO_4
PZT	$\text{Pb}(\text{Zr}_{1-x}\text{Ti}_x)\text{O}_3$
relaxor-PT	$\text{Pb}(\text{BiB}_{11})\text{O}_3\text{-PbTiO}_3$ system
FeRAM	ferroelectric random-access-memory device
3D	three dimensional
P	polarization intensity
E	electric field intensity
P_r	remnant polarization
E_c	coercive electric field
T_c	Curie temperature
ϵ_r	dielectric constant
$\tan\delta$	dielectric loss factor
J	leakage current density
FN	Fowler-Nordheim tunneling
SCLC	space-charge-limited current

PF	Poole-Frenkel effect
RE	rare earth element
TM	transition metal
G-K	Goodenough-Kanamori rule
CSD	chemical solution deposition method
XRD	X-ray diffraction
SEM	scanning electron microscopy
TFL	trap-filled-limit conduction

1.0 Introduction

Ferroelectric materials and their applications are one of the most popular research topics in technology and theory of condensed matter physics and solid-state electronics, due to the fact that they show robust spontaneous polarization which can also be reversible when subjected to external electric fields. With the rapid development of the semiconductor and integrated circuit technology, there is a great increase in demand for high-quality thin-film materials¹. Obviously, some ferroelectric bulk materials can no longer adapt to the current working environment¹. The research on looking for better ferroelectric thin-film materials is urgent.

The bismuth-layered Aurivillius $(\text{Bi}_2\text{O}_2)_{2+}(\text{A}_{n-1}\text{B}_n\text{O}_{3n+1})_{2-}$ materials have been revived in recent years because of the coexistence of ferroelectric ordering and magnetic ordering². At the present stage, their common structural, electric, magnetic, and optical properties have also been systematically investigated in both ceramic and film forms. In order to improve their ferroelectricity, photovoltaic, or magnetic property, most of researchers chose to dope these materials with some transition metals (TM) and rare earth elements (RE) like Cr, Mn, La, and Ho, to eliminate the effect of oxygen vacancies and ionic valence fluctuation, or narrow the band-gap for regulating the ferroelectricity-induced photovoltaic effect³⁻⁶.

In terms of the amount of research devoted so far to Cr-doped $\text{Bi}_5\text{FeTi}_3\text{O}_{15}$ (BFTO, $n=4$) materials, just a little work related to their structural and electrical characterization has been done. Most of their research projects were also bulk ceramics¹⁻⁶. In consideration of the necessity of

deeply exploring properties of ferroelectric thin films and the potential of Cr-doping according to the good results of previous studies in BiFeO_3 materials, it is meaningful to analyze the performance of Cr-doped $\text{Bi}_5\text{Cr}_x\text{Fe}_{1-x}\text{Ti}_3\text{O}_{15}$ thin films⁷⁻⁹. Therefore, we tried to explore the behavior of the bismuth-layered Aurivillius $\text{Bi}_5\text{FeTi}_3\text{O}_{15}$ multiferroic thin films with different Cr-doping content in detail in this article. The crystal structure and microstructure development were monitored, and their influence on ferroelectric and dielectric properties was investigated. This work aimed to find out the impact of Cr-doping on the crystal structure, microstructure and functional properties of $\text{Bi}_5\text{FeTi}_3\text{O}_{15}$ multiferroic thin film.

2.0 Background Information and Literature Review

2.1 Ferroelectric Materials

2.1.1 Ferroelectric Materials Development History

A long time ago, some interesting materials with temperature related self-generating dipole distance were initially discovered. In 1824, Brewster observed that many ores had pyroelectric properties¹⁰. In 1880, the Curies found that when their sample was stressed, the phenomenon of electrode appeared¹¹⁻¹². However, none of these early found pyroelectrics was ferroelectric material. In untreated ferroelectric single crystal materials, the polarization direction of domain was disordered, the total polarization of crystal was zero, the pyroelectric response and piezoelectric response were both pretty small, which caused the discovery of ferroelectricity to be delayed for a long time¹³.

The concept of ferroelectricity was first generated in Rochelle salt $\text{NaKC}_4\text{H}_4\text{O}_6 \cdot 4\text{H}_2\text{O}$ by Valasek at a meeting in 1920, which opened the prelude to the study of ferroelectric materials. And the reason why it was named so because of its similarity to ferromagnetism, which is a magnetic property of a material that has a permanent magnetic moment¹⁴. This set two milestones: (i) showing spontaneous and sustained polarization of Rochelle salt and (ii) showing relation curve between electric charge and electric field¹⁵.

With the continuous understanding and research of ferroelectric materials, some ferroelectric materials with great influence on manufacturing industry came into being after observing the ferroelectricity of Rochelle salt¹⁵. In 1935, Busch discovered something special about potassium dihydrogen phosphate KH_2PO_4 (KDP). Its relative permittivity was as high as 30 that was much higher than other materials at that time¹⁶⁻¹⁸. After 1940, the perovskite-structure ferroelectric materials represented by barium titanate BaTiO_3 (BTO) were discovered during the Second World War, which was also a milestone period in ferroelectric history¹⁹⁻²⁰. Then, the lead zirconate titanate $\text{Pb}(\text{Zr}_{1-x}\text{Ti}_x)\text{O}_3$ (PZT) was discovered by B. Jaffe et al. in 1955 with high Curie temperature at that time, which greatly promoted the development of ferroelectric materials²¹.

Until the 1980s, with the gradual improvement of ferroelectric phenomenological theory and soft-film theory, the research on the physical connotation of ferroelectric materials tended to be stable. In the mid-1980s, the breakthrough of thin-film preparation technology paved the way for the preparation of high-quality ferroelectric thin films²². In recent years, with continuous improvement of the requirements for device miniaturization, functional integration and reliability, the traditional ferroelectric bulk materials can no longer meet the requirements of microelectronic devices due to size limitations^{1, 11, 13, 19}. The research of ferroelectric thin films becomes more and more vital because of the transition of ferroelectric materials to film size and the combination of semiconductor technology.

2.1.2 Applications of Ferroelectric Materials

Ferroelectric materials are a well-known category of dielectric and piezoelectric materials with superior performance today and ferroelectric materials have superior pyroelectric, piezoelectric, and dielectric properties than non-ferroelectric materials²¹, as shown in Figure 1. Since the discovery of BTO in the 1940s, PZT in the 1950s, and relaxor-PT single crystals $(1-x)\text{Pb}(\text{BiB}_{11})\text{O}_3-x\text{PbTiO}_3$ ($\text{Pb}(\text{BiB}_{11})\text{O}_3\text{-PbTiO}_3$ system) in the 1980s, perovskite-structure ferroelectric materials have become the dominating materials for electromechanical devices and have been widely used in sensors, actuators, and ultrasonic transducers, such as therapeutic ultrasonic transducers, large displacement actuators, sonar projectors, and high-frequency medical imaging transducers²¹.

Moreover, ferroelectric materials have the potential to use as environmental-friendly energy storage materials like non-volatile Ferroelectric RAM (FeRAM) device²³. People have investigated the mechanisms of energy losses in electromechanical devices and are trying hard to control and minimize them in order to reduce the degradation of performance. Innovations in electromechanical devices continue to be the driving force for the products of new ferroelectric materials²². Improving the performance of micro ferroelectric devices has been still the most challenging thing so far. For instance, for really high-frequency ultrasonic transducers, the dimension of each element should be down to micrometer so that the sensitivity and accuracy are very significant²².

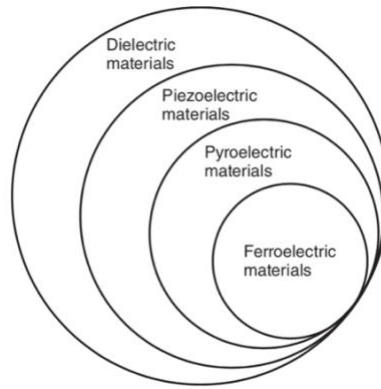


Figure 1. Interrelationship Among Piezoelectric, Ferroelectric, Pyroelectric, and Dielectric Materials²⁴.

2.1.3 Multiferroic Materials

Multiferroics are a class of multifunctional materials characterized by the coexistence of at least two characteristics in the same phase, such as ferroelectric, ferromagnetic, or antiferromagnetic. In the last 20 years, key technological breakthrough in theory, synthesis, and characterization techniques has produced a revival of interest in concerning the study and applications of such highly desired materials, due to the coupling between the magnetic and ferroelectric orders might induce novel functionalities²³. Important attention was paid to the investigation of epitaxial ferromagnetic/ferroelectric heterostructures, multilayers, superlattices, and 3D artificially grown composites for potential applications as multistate field effect transistors, magnetic sensors, and tunneling junctions²⁴. Recently among popular multiferroic candidates, BiFeO₃ (BFO) has emerged as one of the most studied due to its antiferromagnetic property with

a Neel temperature about 370°C and ferroelectric property with a high Curie temperature of about 810°C. However, BFO crystals, whatever ceramics or thin films, suffer from high leakage current density at room temperature which is related to oxygen vacancies and valence fluctuation of Fe ions²⁵.

2.1.4 Aurivillius Phase Materials

Aurivillius phases, also called Bi-based layer structure materials, with the general formula $(\text{Bi}_2\text{O}_2)_{2+}(\text{A}_{n-1}\text{B}_n\text{O}_{3n+1})_{2-}$ (where A = Bi, K, Sr, Ba, Pb... and B = Ti, Fe...) have a naturally layered perovskite-related crystal structure that consists of perovskite-like $(\text{A}_{n-1}\text{B}_n\text{O}_{3n+1})_{2-}$ layers interleaved between fluorite-like $(\text{Bi}_2\text{O}_2)_{2+}$ layers, where n refers to the number of perovskite-like layers, which can be odd, even or a mixture, as shown in Figure 2. For example, we can produce Bi_2WO_6 (n = 1) and $\text{Bi}_4\text{Ti}_3\text{O}_{12}$ (n = 3), or $\text{Bi}_3\text{TiNbO}_9$ (n = 2) and $\text{CaBi}_4\text{Ti}_4\text{O}_{12}$ (n = 4). The example for a mixture Aurivillius material is $\text{Bi}_7\text{Ti}_4\text{NbO}_{21}$. In this case, layers with 2 or 3 pseudo-perovskites are alternated with the $(\text{Bi}_2\text{O}_2)_{2+}$ layers²⁶.

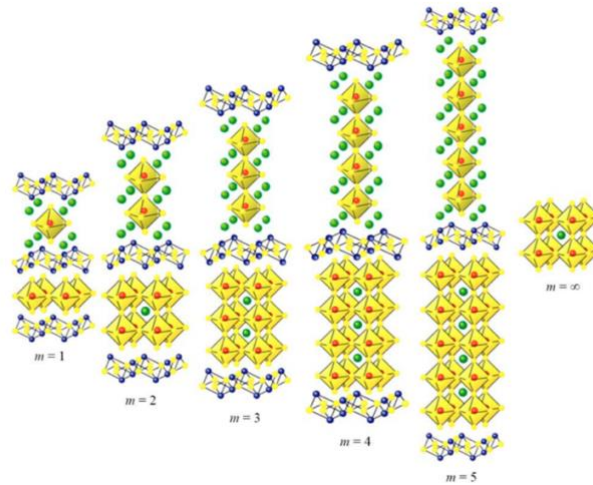


Figure 2. Prototype of the Aurivillius Structure as a Function of the Number of Pseudo-perovskite Layers⁹.

Bi-based layer structure materials pioneered by Aurivillius about seventy years ago have been revived currently because of the fatigue-free behavior, lead-free behavior, and high Curie temperature, regarded as a good candidate in FeRAM devices and high-temperature piezoelectric sensors⁹. Furthermore, Aurivillius structures have been proposed as good candidates for use as single phase multiferroic materials due to their high ferro-paraelectric phase transition temperatures and the ease hosting of magnetic cations in the structure. Multiferroic properties of the coexistence of ferroelectric and magnetic orderings in one phase can be realized by inserting the typical BiFeO₃ phase into the isostructural Bi₄Ti₃O₁₂25. More importantly, an associated magnetoelectric coupling between spin and dipolar orderings leads them to be qualified in high-speed and low-power consumption multistate memory⁹, spintronics devices, and even photovoltaic cells⁷.

The first Aurivillius phase ferroelectric material was $\text{PbBi}_2\text{Nb}_2\text{O}_9$, discovered by Smolenski and Agranovskaya in 1959. After that, Smolenski et al. and Subbarao confirmed ferroelectric properties for plenty of Bi-based layer structure materials with the general formula above. Combined with fatigue-free behavior, good retention characteristic and lower leakage current density, $\text{SrBi}_2\text{Ta}_2\text{O}_9$ -based ($n=2$) Aurivillius compounds were also commercialized as FeRAM by Ramtron in the 1990s⁹.

2.1.5 $\text{Bi}_5\text{FeTi}_3\text{O}_{15}$ and Thin Film Ferroelectric Materials

The Bi-based layer Aurivillius phase ferroelectric materials with higher n has been received more attention in recent years not merely because new physical natures were found but also advanced preparation technology²⁶. To be more explicit, this reason is not only due to the admirable abundance with fundamental physics (mainly focused on the coexistence of ferromagnetism, ferroelectricity, and high ferroelectric phase transition temperatures), but also the huge application potential as multilevel memory storage media, emergent spintronic technologies, energy harvesting, sensors and actuators^{23, 26}. Relative high values of remnant polarization P_r between 13 and 16 $\mu\text{C}/\text{cm}^2$ have been achieved in $\text{Bi}_6\text{Fe}_{2-x}\text{Co}_x\text{Ti}_3\text{O}_{18}$ solid solutions and $\text{Bi}_5\text{FeTi}_3\text{O}_{15}$ compound⁹.

The Aurivillius phase $\text{Bi}_5\text{FeTi}_3\text{O}_{15}$ consists of perovskite-like $(\text{Bi}_{n-1}\text{FeTi}_{n-1}\text{O}_{3n+1})_2$ ($n=4$) octahedral layers interleaved between two fluorite-like $(\text{Bi}_2\text{O}_2)_{2+}$ layers along c axis, where the n refers to the number of perovskite-like layers²⁶. The perovskite-like Fe/Ti–O octahedral layers are

responsible for the ferroelectricity and the ferromagnetism. The origin of ferroelectricity in the Aurivillius family is a combined effect of octahedral rotations and polar distortions. The polarization is mainly showed along a-axis in a-b plane. The displacements of ions along the a-axis in the perovskite-type units are the main cause of the large polarization²⁷⁻²⁸. The polarization along the c-axis is quite small, because the buckling of the octahedra along the c-axis almost cancels the dipole moments²⁸⁻³⁰. The fluorite-like $(\text{Bi}_2\text{O}_2)_{2+}$ layers always determine the reinforced resistance²⁶. The Curie temperature T_c was determined to be about 730°C.

On the other hand, new phenomenological theories were formulated to describe ferroelectric materials more accurately, and countless applications in thin-film form have occurred in the past 60 years¹. By the 1960s, initial studies of ferroelectric films were undertaken to realize non-volatile memory function, but difficulty in producing high-quality films limited their use until the 1980s¹. By the 1990s, ferroelectric thin films were finding widespread application in memory devices, radio frequency and microwave devices, pyroelectric (thermal) and piezoelectric (stress) sensors and actuators^{1, 3, 4}.

It is tough for bulk ferroelectric materials to reach the needed poling due to the high coercive field, which might be a big drawback for the potential applications. In this case, the use of thin films can overcome this issue. By reducing the thickness of the material, lower voltages are needed to apply a high electric field. This can help to facilitate the films integration in microelectronic devices, expanding the applicability of this material family.

2.2 Ferroelectric and Dielectric Properties

2.2.1 Spontaneous Polarization in Ferroelectrics

In a certain temperature range, the positive and negative charge centers in the unit cell do not coincide, then forming a dipole moment, finally showing polarity. This phenomenon is called spontaneous polarization as shown in Figure 3. The most basic ferroelectricity refers to the spontaneous polarization of materials in this certain temperature range. When the external electric field is applied, the direction of spontaneous polarization in each unit cell tends to be same along the electric field direction; when the external electric field is reversed and exceeds the coercive electric field E_c of the material owns, the spontaneous polarization reverses along with the electric field; when the electric field is removed, part of the polarization retained in the material, namely the residual polarization^{11, 13, 15, 27}.

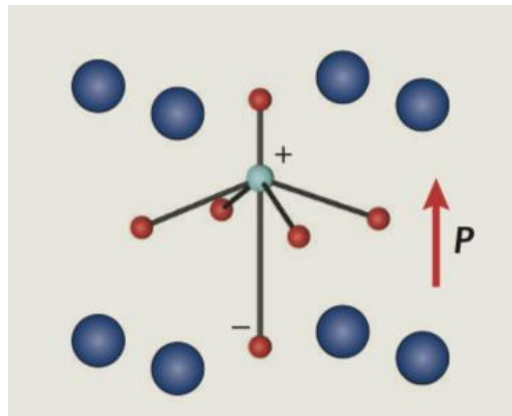


Figure 3. Spontaneous Polarization Model.

There is an obviously hysteretic relationship between spontaneous polarization and electric field. Electronic ceramics, such as capacitors and sensitive components, can be made with this characteristic¹⁴. When the spontaneous polarization changes the direction under the action of the external electric field, the hysteresis loop occurs. When the temperature is higher than a critical value, the lattice structure changes, the positive and negative charge centers coincide, and the spontaneous polarization will disappear. This critical temperature is called Curie temperature T_c , as shown in Figure 4.

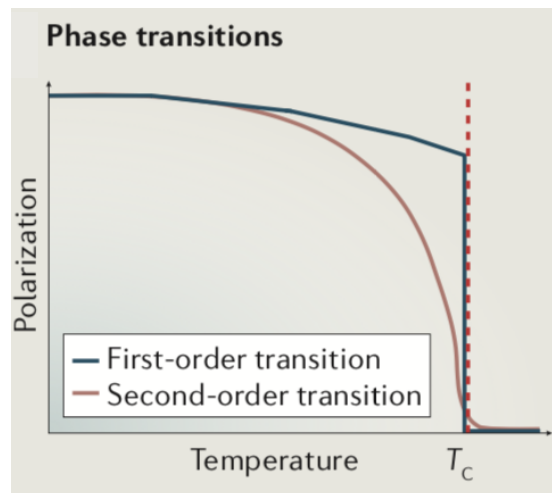


Figure 4. The Normal Relationship Between Polarization and Temperature.

2.2.2 Ferroelectric Domains and P-E Hysteresis Loop

In general, many different directions of spontaneous polarization exist in the whole ferroelectrics, but in a small area, the direction of spontaneous polarization of each cell is same. This small area is called ferroelectric domain, and its linearity is in the order of micrometer. In one ferroelectric domain, the orientation of each small electric dipole moment is same. And the spontaneous polarization direction of different ferroelectric domains is generally different, so the total electric dipole moment is zero^{9, 11, 13, 16, 17}. If it is polycrystalline, the orientation of the grains themselves is arbitrary, and the relative orientation of polarization intensity in different domains can be irregular. However, if it is a single crystal, there is a simple relationship between the polarization intensity orientations in different domains.

The boundary between two domains is called domain wall. If the spontaneous polarization directions of two domains are 90° to each other, the domain walls are called 90° domain walls. In addition, there are also 180° domain walls²⁷. Under the external electric field, the polarization direction of each ferroelectric domain tends to be the same, and the relation curve between polarization intensity P and electric field intensity E is called hysteresis loop. When the T_c is reached, the ferroelectric domain will be separated from each other, and the ferroelectric property will disappear. Finally, this ferroelectric will be transformed into paraelectric dielectric.

Generally speaking, the spontaneous polarization property of a ferroelectrics is determined by the asymmetry of the crystal structure. However, the feature that the external electric field can

make the spontaneous polarization reverse cannot be predicted by the crystal structure and can only be judged by the measurement of the hysteresis loop like Figure 5. The hysteresis loop indicates the presence of ferroelectric domain in the material.

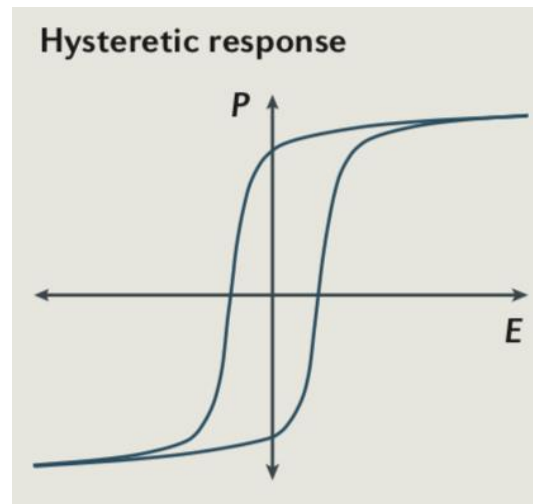


Figure 5. The Classic Hysteresis Loop¹.

2.2.3 Dielectric Constant and Loss Factor

Dielectric constant ϵ_r , the physical parameter that characterizes the dielectric property or polarization property of the dielectric material. It numerically equals the ratio of the capacitance of the same-size capacitor made of the tested material and the vacuum medium, which is also the characterization of the material's capacity of energy storage^{18, 22, 27}. Dielectric constant physically reflects the electrostatic force between two point charges in the material. The greater the dielectric

constant, the smaller the Coulomb interaction between point charges. Taking the silicon solar panel as an example, the dielectric constant of silicon is more than 10, so the electron-hole pairs produced in silicon are easy to separate and form free charges.

Due to the nonlinearity of polarization, the dielectric constant of ferroelectric material is not fixed, but strongly depends on the external electric field. Generally, the dielectric constant of a kind of ferroelectrics is relatively large near its Curie temperature. When the temperature keeps getting higher, the relationship between the dielectric constant and this temperature follows the Curie-Weiss law^{18, 22, 27}.

Dimensionless dielectric loss tangent value $\tan\delta$ (dielectric loss factor) is often used to describe the magnitude of dielectric loss. It originates from the phenomenon that the dielectrics itself heats up due to the consumption of part of electric energy under the alternating electric field. The dielectrics contains some carriers that make material itself conductive. Under the strong action of external electric field, the current is generated which consumes part of electric energy due to thermal motion and turns into heat inevitably. Dielectric Loss normally includes leakage loss, ionization loss, polarization loss and structure loss. The value of dielectric loss factor is related to material composition, working frequency, ambient temperature, humidity, load size and acting time^{18, 22, 27}. For general dielectric materials, the smaller the loss is, the better the performance is.

2.2.4 Leakage Current in Ferroelectric Thin Films

For metal–ferroelectrics–metal configuration, impurity ion conductance and extrinsic defects carrier conductance are the main factors influencing the thin-film conductivity at room temperature^{28, 29, 30}. For instance, oxygen vacancies are widely reported as one of the major origins for many n-type ferroelectric materials' conductivity²⁶. The increase of oxygen vacancies owing to the growth of the crystallite size and the decrease in grain boundaries as well, will lead to the increasing of leakage current density J . Furthermore, for the p-type BFTO material, the hole carriers are created by valence fluctuation of Fe^{3+} to Fe^{2+} , resulting in leakage current density J increasing. Such valence-relative conductance is remarkable in the p-type insulators²⁶.

In addition, the leakage current mechanism between electrodes and thin films was studied by various conduction mechanisms. The common conduction mechanisms can be ascribed to interface-limited conduction²⁶: Schottky emission and Fowler-Nordheim tunneling (FN); bulk-limited conduction: space-charge-limited current (SCLC) and the Poole-Frenkel effect (PF).

2.3 Doping Effect in Ferroelectrics

2.3.1 A Change in Multiferroic Property by Impurity Doping

A route followed during several years to enhance the performance of ferroelectric materials is the impurity doping method. An increasing number of researchers have improved ferroelectric and ferromagnetism properties via substitution of RE ions at A-site and TM ions at B-site. For

BFO perovskite structure, Mn^{2+} , Ho^{3+} , La^{3+} , Mn^{4+} , and Ti^{4+} ions had been doped into the A-site or B-site of BFO lattice system to reduce oxygen vacancies and decrease the lattice distortion²⁸⁻³⁰. The reason for the improvement by doping is the enhancement in local lattice due to fewer defects, as oxygen vacancies in the perovskite layers, which reduces the electrical conductivity²⁻⁶. This leads to an increase of remnant polarization by reducing the leakage current density.

Meanwhile, others have combined two single phase multiferroic materials to enhance magnetoelectric polarization, but the doping engineering possesses a prominent advantage comparing with the combination. It provides an effective internal approach to induce the magnetoelectricity domain switching behaviors.

2.3.2 A Change in Multiferroic Property of Aurivillius Phases by Impurity Doping

Among multiferroic materials, the Aurivillius phases like $Bi_5FeTi_3O_{15}$ have been the focus of remarkable interest in their application²⁰. The ferroelectricity in these materials is mainly attributed to the perovskite-like layers; the fluorite-type ones block the ion migration and reduce the pooling fatigue, improving their leakage behavior and dielectric performance²⁶. The past results indicated that the multiferroic properties of Aurivillius phases still suffered from low electrical resistivity and high leakage current density, deteriorated by the effects of ionic valence fluctuation, oxygen vacancies and large lattice distortion, which limited the use in multiferroic functional devices^{2-6, 22}.

2.3.3 Cr-doping Effect

To well-investigated BFO materials, among various kinds of doping reported at B-site, Cr-doping was found especially attractive due to the smaller lattice distortion in BFO caused by smaller Cr³⁺ radius (0.615Å) than Fe³⁺ radius (0.645 Å)³¹⁻³². After small amount of Cr-doping, caused by smaller Cr³⁺ radius (0.615Å), the tolerance factor of BFO increases and then restricts the lattice distortion. Because of the resistivity to oxidation and reduction, the adding of Cr³⁺ suppresses the formation of oxygen vacancies and subsequently lowers the conductivity, which can improve the ferroelectricity³²⁻³³.

To well-known BFTO multiferroic material, several papers showed that no obvious signs of the improvement in ferroelectric properties were found and abnormal P-E hysteresis loops were observed as Cr-doping content was beyond 0.12, ²⁴. However, the effects of Cr-doping on the crystal structure, electric transport, and dielectric/ferroelectric properties of BFTO thin films are still inconclusive in the present literatures, even though there are some informative but incomprehensive studies^{2, 22, 25}. Therefore, we want to conduct a comprehensive analysis and research in detail in this article. This work aimed to find out the impact of Cr-doping on the crystal structure, microstructure and functional properties of Bi₅FeTi₃O₁₅ multiferroic thin film. It is probable that the certain amount of Cr-doping will bring positive influence on ferroelectricity that is similar as the Cr-doping effect on BFO materials due to the smaller lattice distortion.

3.0 Research Description

3.1 Hypothesis

Given that Cr-doping modify the ferroic properties of BFO films, the hypothesis of this study is that a decrease in the structural distortion in Cr-doped BCFTO may change the ferroelectric properties of BFTO film.

3.2 Objectives

In order to find out whether the Cr-doped BCFTO thin film show better ferroelectric property than pure BFTO thin film, we conduct comprehensive research to find out the impact of Cr-doping on the crystal structure, microstructure and functional properties of BFTO.

3.3 Tasks

The change of the magnitude of saturated polarization P_s and remnant polarization P_r verse external electric field E , and different coercive field E_c values should be compared. At the same time, the corresponding leakage current density J verse E need to be calculated. Combined with the result of dielectric, crystal structure, and microstructure, the effect of Cr-doping on structure, dielectric, and ferroelectric property can be clearly found out.

During the experiment, the first key point is to produce high-quality BCFTO thin films in order to make results more credible. It is known to all that the chemical solution deposition

technique which is used as this study's processing method is a frequently used but not high-precision technique. Generally, compared with pulsed laser deposition technique, our thin films will be made more easily but have more defects.

The second key point of this study is to ensure all measurement of thin films' properties is done under relatively same conditions. The measurement of thin film materials will probably be affected by many anthropic factors, like the pressure given by positive and negative probes when doing the ferroelectricity measurement.

4.0 Experiment Details

4.1 Precursor Preparation

$\text{Bi}_5\text{Cr}_x\text{Fe}_{1-x}\text{Ti}_3\text{O}_{15}$ thin films were prepared by chemical solution deposition method (CSD) (hereafter abbreviated as BCFTO and also denoted as BFTO for $x=0$, $\text{BC}_{0.1}\text{F}_{0.9}\text{TO}$ for $x=0.1$, $\text{BC}_{0.3}\text{F}_{0.7}\text{TO}$ for $x=0.3$, and so on). Bismuth(III) acetate, iron(II) acetate, titanium(IV) n-butoxide, and chromium(III) acetate hydroxide in stoichiometric proportions were mixed thoroughly with 5 mol% excess bismuth acetate, used to compensate the volatile-Bi loss that was induced during the thermal annealing of amorphous films. Then the mixing raw material was put in propionic acid solution, and they were further stirred using a magnetic stirrer at room temperature for more than 6 hours.

4.2 Coating and Annealing Procedure

As shown in Figure 6, thin films were deposited onto commercial $7\text{mm} \times 7\text{mm}$ polycrystalline Pt/Ti/SiO₂/Si/ substrates. These new substrates were successively cleaned by acetone, ethanol, and deionized water in ultrasonic baths. The coating procedure was performed at ambient atmosphere with a rotation speed of 5000rpm and a time of 20s, followed by a drying process at 150°C for 2min and a pyrolysis process at 400°C for 10min in air. The processes of spin-coating and pyrolysis were repeated six times to increase the thin film thickness. Then, the baked films were annealed in a 650°C preheated tube furnace (OTF-1200X, MTI) in air

atmosphere for 30min. The annealing temperature 650°C is moderate to films and substrates according to another past research²⁵. The final thickness of each film is approximately 400nm, according to the corresponding cross section profile obtained by scanning electron microscopy.

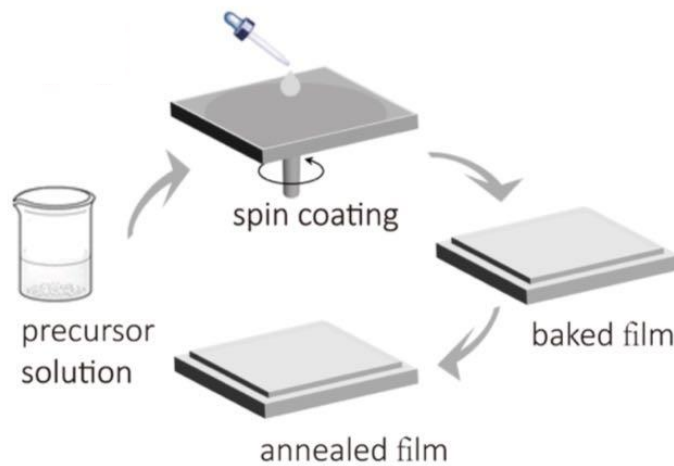


Figure 6. The Procedure of Ferroelectric Thin Films' Preparation²⁶.

4.3 Electrode Deposition

In order to measure the ferroelectric and dielectric properties of these films, 80nm-thick gold dot top electrodes with the diameter of 0.2mm were deposited by e-beam plassys through a shadow mask.

4.4 Crystal Structure and Bandgap

4.4.1 X-ray Diffraction Test

The crystalline phases of the films were analyzed by X-ray diffraction (XRD, Panalytical Empyrean) with Cu-K α radiation at room temperature.

4.4.2 Ultraviolet-visible Spectroscopy Test

Another group of five thin films in same composition and preparation process were coated on FTO glasses. And then the optical absorption spectrum was measured by an ultraviolet–visible spectrometer (Lambda 35, PerkinElmer).

4.5 Microstructure and Ferroelectric Property

4.5.1 Scanning Electron Microscope Test

The surface microstructure, the grain growth, and change in the microstructure of the films were observed by scanning electron microscopy (SEM, JEOL 6610LV, FEI Apreo).

4.5.2 Ferroelectric Property Measurement

The hysteresis loop measurements were carried out using a Precision Materials Analyzer (Precision RT66C, Radiant Technologies).

4.6 Dielectric Property and Leakage Current Density

4.6.1 Dielectric Property Measurement

Dielectric properties were performed with a high-performance impedance analyzer (IM3570, HIOKI).

4.6.2 Leakage Current Measurement

Leakage current measurements were also carried out using a Precision Materials Analyzer (Precision RT66C, Radiant Technologies).

5.0 Result and Discussion

5.1 Crystal Structure and Bandgap (Composition Effect)

Figure 7(a) shows XRD patterns of the substrate and Cr-doped BCFTO samples from $x=0$ to $x=1$. All these samples demonstrate almost identical XRD profiles and are consistent with the diffraction data of BFTO in other literatures^{2, 24}, in accordance with the standard peaks of Aurivillius BFTO phase. In addition, no significant change in the XRD patterns of the BCFTO samples with different Cr concentration are observed. This indicates that Cr-doping would not modify the overall crystal structure with Aurivillius phase, implying a large solid solubility of Fe and Cr in our samples. Most of Cr ions complete the substitution successfully. The lattice parameter c is shown in Figure 7(b). It's calculated with the help of MDI Jade software. The calculation principle used is the interplanar spacing equation.

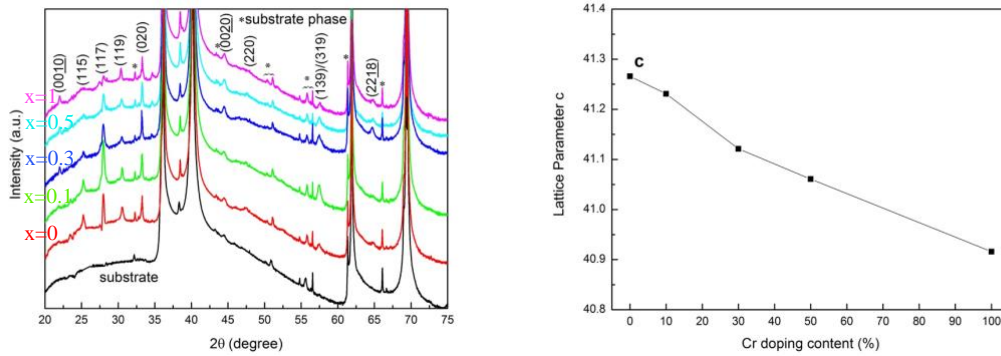


Figure 7. (a) XRD Patterns, Plotted as Log Intensity Versus 2θ , of the Substrate and the $\text{Bi}_5\text{Cr}_x\text{Fe}_{1-x}\text{Ti}_3\text{O}_{15}$ Thin Films for $x=0, 0.1, 0.3, 0.5,$ and 1 from the Bottom Up (b) A Change in the Lattice Parameter of C-axis With Different Cr-doping Content.

In order to investigate the effect of Cr content on the BFTO crystal structure, the detailed XRD patterns of 2θ around the diffraction peak located at (200/020) is depicted in Figure 8(a). First of all, this diffraction peak (200) shifts to right side toward the higher angle and shifts back to left side with the continuous increase of Cr-doping. This phenomenon is due to the dimensional change that the ionic radius of Cr^{3+} (0.615\AA) is smaller than that of Fe^{3+} (0.645\AA)^{2, 37-40}. This further proves that the crystal lattice parameter a and b should change with the increase of Cr content.

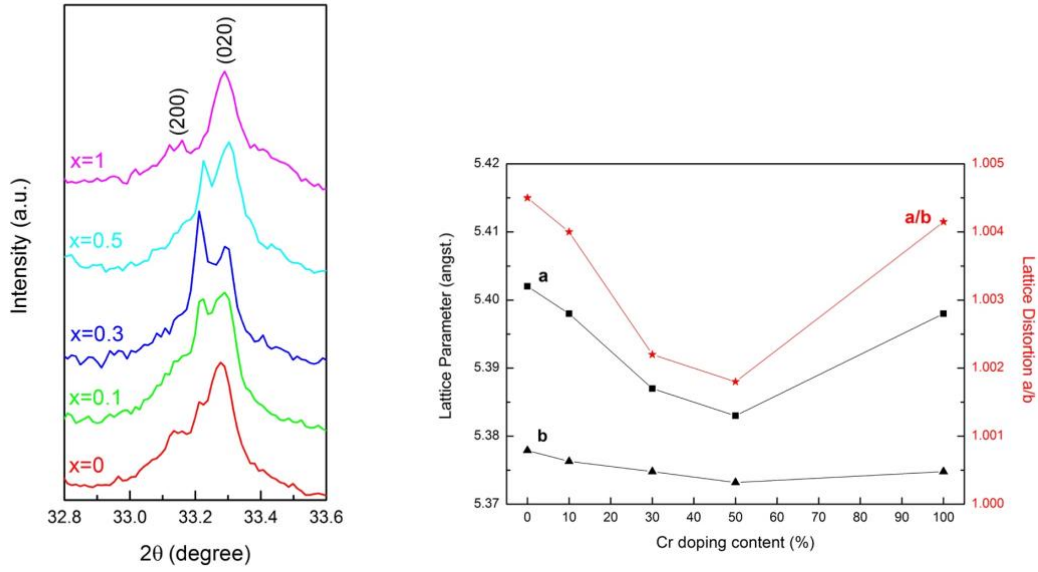


Figure 8. (a) Local Broadened XRD Pattern of 2θ Around the Diffraction Peak Located at (200/020) (b) The Variation of the Lattice Parameters a, b, and Lattice Distortion a/b of Samples with Cr-doping Content.

To be more explicit, the variation of the lattice parameters a, b, and lattice distortion a/b with Cr-doping content are plotted in Figure 8(b). The lattice distortion a/b slightly decreases and then increases as the doping of Cr, which is similar from that of BFO material^{2, 31-34}. According to Jia Liu and his team², the suppression of lattice distortion of Cr ions substitution for Fe ions is existed in BFTO material. The smaller lattice distortion might be due to the doping effect of smaller radius of Cr^{3+} , indicating that the disordered mixing of Cr and Fe may reduce the formation of the long-range distortion which is closely related to ferroelectric polarization. When the Cr-doping content is over 0.5, the lattice distortion further increases again, since it will not a great solid solution anymore. This phenomenon might affect the ferroelectric property by reducing a

formation of residual strain during a transition from a paraelectric phase to a ferroelectric phase, which is further discussed in the next part.

The ultraviolet–visible absorption spectrum in the wavelength range of 200~700 nm for all BCFTO films are shown in Figure 9(a). Their approximate bandgap values can be calculated by Tauc relation in Equation 5-1 and Equation 5-2:

$$\alpha hv = C(hv - E_g)^n \quad (5-1)$$

and

$$\alpha = (1/d)\ln (1/T) \quad (5-2)$$

where α is the absorption coefficient, hv is the photon energy, C is a constant, E_g is bandgap energy, n is 1/2 for direct bandgap semiconductor model, T is transmittance, and d is the film thickness³⁴. Thus, E_g of films can be estimated from the tangent line in the plot of $(\alpha hv)^2$ versus hv , which is the intersection of linear part and horizontal ordinate³⁴⁻³⁶.

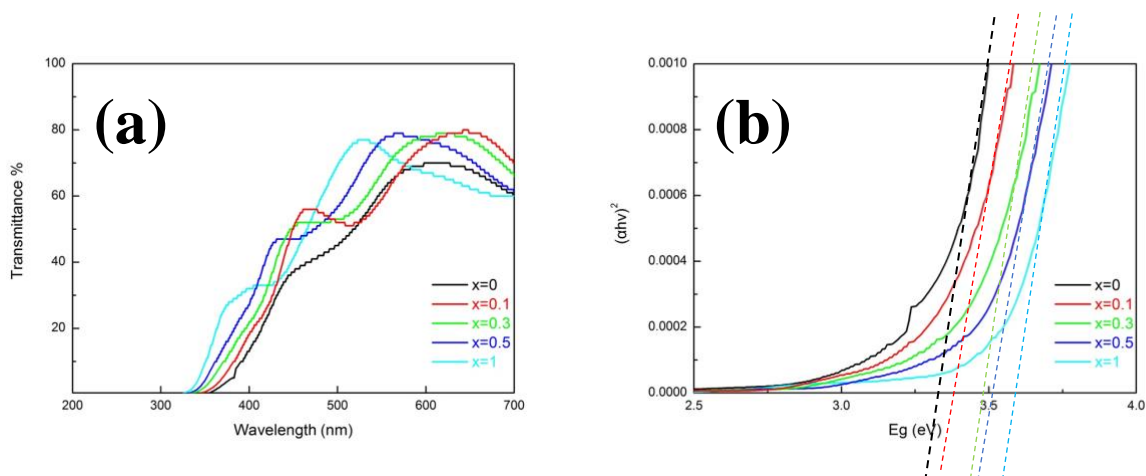


Figure 9. (a) The Ultraviolet-visible Transmittance Spectra for Bi₅Cr_xFe_{1-x}Ti₃O₁₅ Films (b) The Plot of $(\alpha h\nu)^2$ as a Function of Photon Energy Around the Absorption Edge.

As shown in Figure 9(b), the bandgap of BCFTO gradually increases approximately from 3.25eV to 3.6eV with more substitution of Cr ions. The value of the bandgap is actually the minimum energy required for the valence band electrons to transition to the conduction band, and this energy is related to the valence bond energy in band theory^{5-7, 34}. The stronger the bond is, the larger the bandgap is. With the increase of Cr content, the lattice parameter *c* and the lattice volume will decrease due to the smaller radius size of Cr ions^{31, 33}, leading to the larger bandgap in this sense.

5.2 Microstructure and Ferroelectric Property (Shape Effect)

Figure 10 show the typical SEM microstructure of all BCFTO thin films for x=0, 0.1, 0.3, 0.5, 1. It is clear that all samples have relatively dense morphologies and no big pore. Comparing

all samples, the plate-like grains gradually occur in original spherical particles and apparently become larger and thicker with higher doping level. What's special is that the dense plate-like grains dominate the characteristic of microstructure of BCFTO when $x=0.5$, indicating that 50 atomic% Cr-doping completely alter the grain-shape. Finally, the coexist of plate-like grains and spherical grains can be observed clearly when $x=1$, proving the different grain morphology could be related to a change in the lattice distortion in a-b plane.

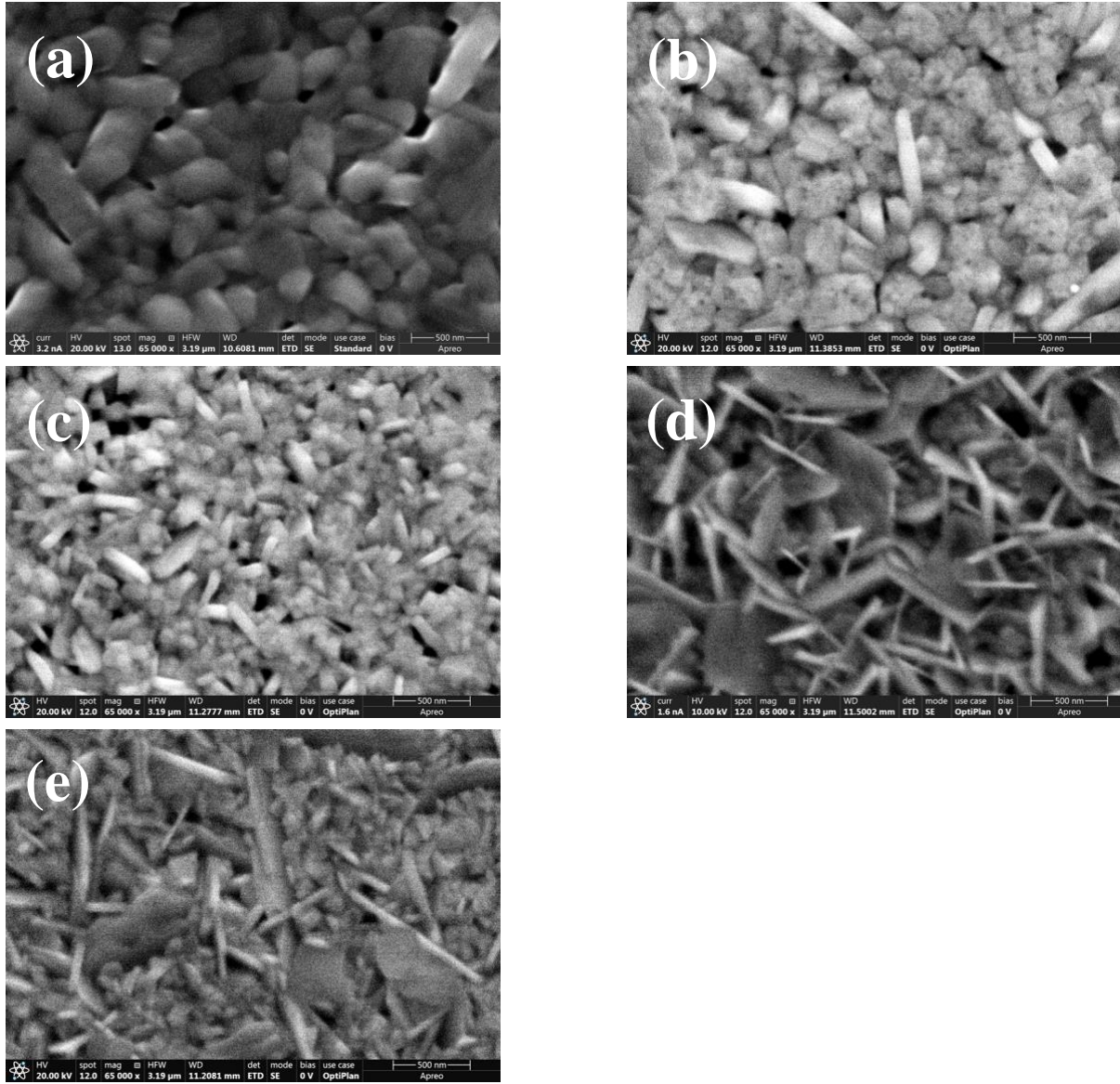


Figure 10. The SEM Images of the $\text{Bi}_5\text{Cr}_x\text{Fe}_{1-x}\text{Ti}_3\text{O}_{15}$ Thin Films for: (a) $x=0$, (b) $x=0.1$, (c) $x=0.3$, (d) $x=0.5$, (e)

$x=1$.

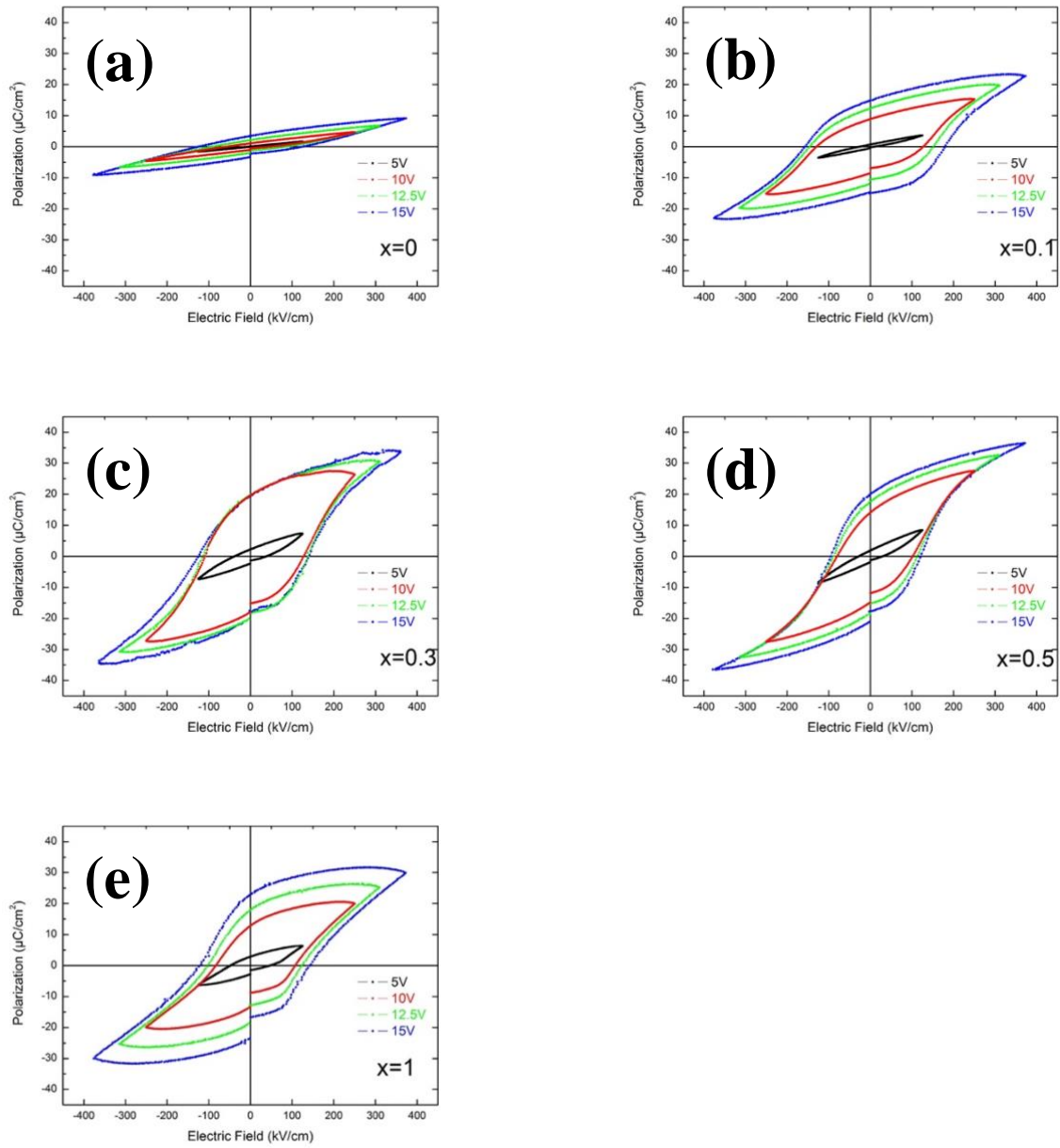


Figure 11. P-E Hysteresis Loops of the $\text{Bi}_5\text{Cr}_x\text{Fe}_{1-x}\text{Ti}_3\text{O}_{15}$ Thin Films at a Measurement Frequency of 100 Hz for:

(a) $x=0$, (b) $x=0.1$, (c) $x=0.3$, (d) $x=0.5$, (e) $x=1$.

Figure 11 shows the room-temperature P-E hysteresis loops of BCFTO samples annealed at 650°C under voltages varying from 5V to 20V with the frequency of 100 Hz. The measurement model is like a typical configuration of a parallel plate capacitor between an evaporation surface Au top electrode and a planar bottom electrode²⁶.

First of all, it can be seen the squareness of the loop of each sample is well improved with increasing applied voltage, which means these thin films showed normal ferroelectricity and relatively good quality under moderate electric field. Secondly, the hysteresis loops of Cr-doped BCFTO samples approach saturation over an applied electric field of 350 kV/cm, but pure BFTO doesn't approach, indicating the high coercive field of BFTO. And it is obvious that the values of remnant polarization P_r and saturated polarization P_s are increasing significantly with the Cr-doping. The values of P_r of pure BFTO and pure BCTO are measured to be about 4.75 $\mu\text{C}/\text{cm}^2$ and 21.00 $\mu\text{C}/\text{cm}^2$, respectively, under a driving electric field of 375 kV/cm, which are similar with the results of other papers⁴¹⁻⁴⁴. The increase of Cr also tends to decrease the sharpness in the shape of hysteresis loop, indicating that a leak current flows during the measurement.

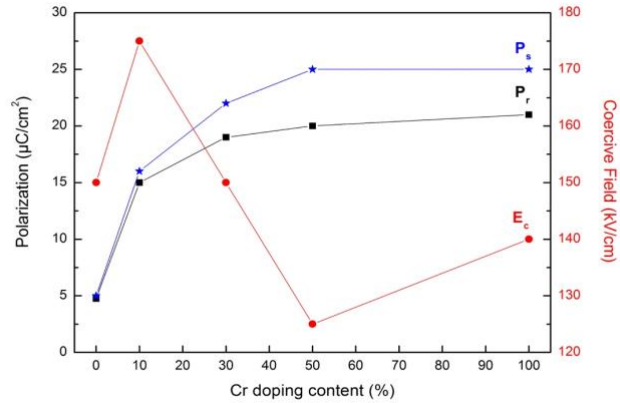


Figure 12. The Variation of the Saturation Polarization, Remnant Polarization and Coercive Field as a Function of Cr-doping Content.

The variation of the saturation polarization, remnant polarization and coercive field as a function of Cr-doping content is plotted in Figure 12. When we focus on the ferroelectricity of those BCFTO samples, it can be found that the ferroelectricity is improved when Cr content is about $x=0.5$. To be more explicit, the values of P_r and E_c of $BC_{0.5}F_{0.5}TO$ are about $20.00 \mu C/cm^2$ and $125 kV/cm$. The shape of loop becomes the sharpest which means the leakage current and the energy loss are not increasing continuously as its polarization grows.

Generally speaking, ferroelectric material is usually composed of many regions with domains, and each domain has the same polarization direction in one region, but it is different from the neighboring domain. For polycrystals, the orientation of polarization in different domains is irregular because the orientation of those grains' growth themselves is arbitrary^{2, 22, 26}. In our

case, the change in the polarization, coercive field and leakage current can be explained using the lattice distortion of a-b plane and the grain shape. On the one hand, the random packing of plate-like grains might make more originally anisotropic ferroelectric domains oriented in a-b plane, and more likely change those domains in same direction under external electric field and showing larger polarization in a-b plane, when $x=0.5$. And due to the smallest lattice distortion and the plate-like grain shape, the formation of residual strain during a transition from a paraelectric phase to a ferroelectric phase is reduced. This suppress the formation of a complicated 3D domain structure consisting of 90° and 180° domain boundaries. This effect facilitates the alignment of ferroelectric domains under electric field without external force which leads to a larger saturated polarization, and the increasing portion of 180° domain boundaries results in a low coercive field. In addition, plate-type grains have less contact area between grains and decrease the leakage current under high electric field in $\text{BC}_{0.5}\text{F}_{0.5}\text{TO}$ thin films.

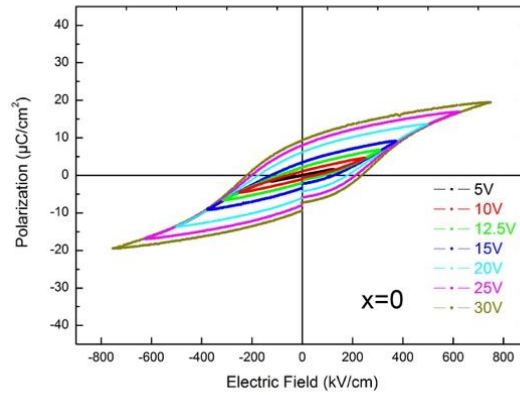


Figure 13. P-E Hysteresis Loops at Different Voltages with the Frequency of 100 Hz of the Pure BFTO Thin Film.

In order to know the best performance of pure BFTO for more detailed comparison, the saturated P-E loop for the BFTO sample is necessarily conducted at room temperature under voltages varying from 5V to 30V with the frequency of 100 Hz. It is clear from Figure 13 that the shape of P-E loop starts to become sharper with increasing driving electric field. Compared with the $\text{BC}_{0.5}\text{F}_{0.5}\text{TO}$ samples, the saturated polarization and the remnant polarization level is still lower. The reason is same as discussed above.

All in all, no obvious improved ferroelectric properties are observed in lightly Cr-doped BCFTO and pure BCTO thin films. However, $\text{BC}_{0.5}\text{F}_{0.5}\text{TO}$ shows a sharp hysteresis loop, large values of remnant polarization and saturated polarization, and the smallest coercive field. Thus, 50 atomic% Cr-doping in the BFTO thin film can improve its ferroelectric property in this case, which

is also similar with the effect of Co substitution in other papers⁴⁴. But further verification is still needed in this respect.

5.3 Dielectric Property and Leakage Current Density (Leakage Behavior)

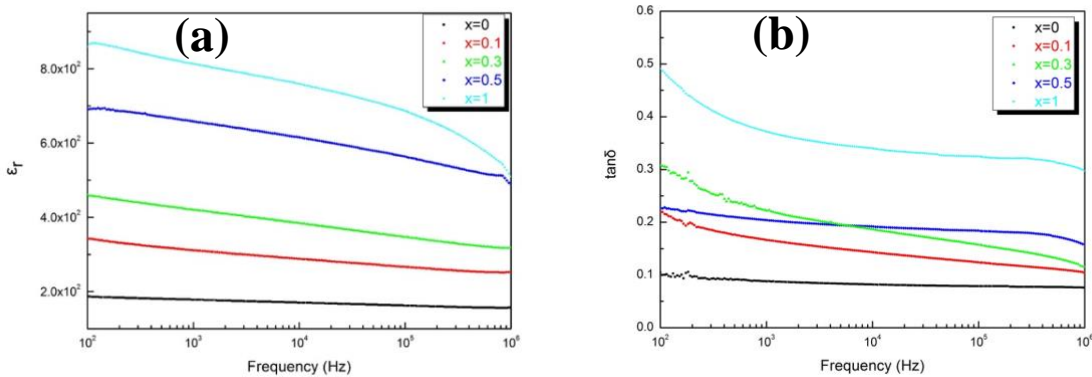


Figure 14. The Frequency Dependences of: (a) Dielectric Constant ϵ_r (b) Loss Tangent $\tan\delta$ for all these BCFTO

Samples.

Figure 14 exhibits the dielectric constant ϵ_r and loss tangent $\tan\delta$ as a function of frequency f ranging from 10² Hz to 10⁶ Hz for all these BCFTO samples under 0.5V external electric field at room temperature. First of all, the value ranges of ϵ_r and $\tan\delta$ at 100 Hz are approximately from 200 to 875 and from 0.1 to 0.5, respectively, which are at reasonable magnitude compared to those similar thin-film ferroelectric materials from other reports^{46, 48}. Furthermore, as shown in Figure 14(a), the more Cr the film has, the greater dielectric constant the film owns. The dielectric constant is a coefficient indicating the insulation capacity. Theoretically,

the greater the dielectric constant is, the better the insulating performance is. Because under the same voltage, the larger the capacitance, the more the charge stored in the capacitor, the more the weakening of the original electric field, the greater the dielectric constant. Generally speaking, this conclusion is true for the comparison between materials with poor insulation and materials with good insulation, but not necessarily for two insulators⁴⁷. In our case, the result indicates that the magnitude of dielectric constant may be related to the increase of hole carrier concentration with the Cr-doping. With the increasing of Cr-doping content, the dielectric constant gradually increases that means more hole carriers create and accumulate in the film. The resulting space charge made a great contribution to the creation of polarization effect inside.

Dielectric loss tangent $\tan\delta$ represents the ratio of the energy of dielectric loss to its storage energy in each work cycle. Obviously, as shown in Figure 14(b), with the increase of Cr content, the magnitude of loss becomes greater and significant dielectric loss decreasing behaviors at low frequency are also observed in Cr-doped BCFTO samples compared with the pure BFTO film, that is, $\tan\delta$ drops dramatically with rising frequency. This confirms that the space charge polarization made a great contribution to the leakage behavior. When Cr content meets the critical value $x=0.5$, the $\tan\delta$ value decreases to approximately 0.225. This trend is also consistent with the previous results of P-E loops. The deterioration of ferroelectric property can be attributed to the leakage current component⁴⁵⁻⁴⁸, which is well reflected in low-frequency dielectric response as shown. The degree of leakage current can be explained from carrier concentration and grain-shape effect.

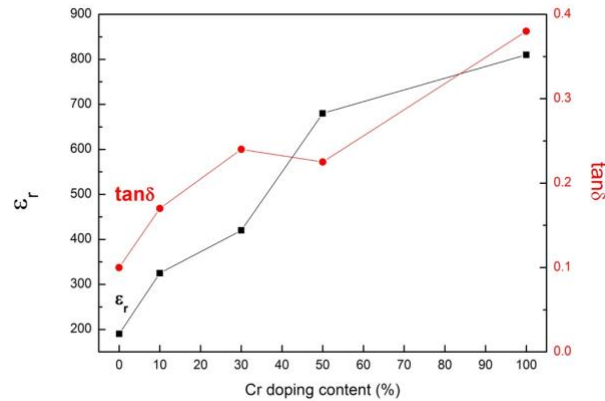


Figure 15. The Variation of the ϵ_r and $\tan\delta$ of Samples at 1kHz with Cr-doping Content.

To be more explicit, the variation of the ϵ_r and loss tangent $\tan\delta$ of samples at 1kHz with Cr-doping content is shown in Figure 15. The free charge carriers of BCFTO thin films are hole carriers (p-type), produced owing to the valence fluctuation of Fe ions from Fe^{3+} to Fe^{2+} during the heat treatment of films^{22, 26, 46}. This suggests that Cr-doping suppresses the oxygen vacancy formation and increases the hole concentration. And the intergranular conduction can be responsible for the leakage behavior of this kind of material²⁶. It has showed in SEM images that when Cr content meets the critical value $x=0.5$, the random packing of the plate-like grains occurs. The contact area between grains decreases to a relatively reasonable magnitude as shown in Fig. 11(d). Plate-type grains have less contact area between grains and decrease the leakage current under high electric field. Although the leakage behavior of $\text{BC}_{0.5}\text{F}_{0.5}\text{TO}$ is still a little bit severer

than pure BFTO thin film, this is acceptable, and the well-enhanced ferroelectric property is what we expect.

Additionally, compared with other Cr-doped BCFTO samples, the dielectric loss decreasing behavior of BC_{0.5}F_{0.5}TO at low frequency becomes much less significant, even showing similar slope as that of pure BFTO. As the discussion above, the less contact area between grains not only decreases the leakage current, but also prevents the appearance of space charge polarization. This significantly eliminates the energy loss created by the space charge at low frequency.

Figure 16 and Figure 17 below show the dielectric constant ϵ_r and loss tangent $\tan\delta$ as a function of frequency f ranging from 10^2 Hz to 5×10^6 Hz for all these BCFTO samples under 0.5V external electric field at various temperatures from room temperature 298K to 423K. They show temperature dependence. Firstly, taken together, the result of each sample shows same tendency with increasing working temperature. The higher the temperature is, the larger ϵ_r the film shows, as well as the loss tangent. Notable increase in ϵ_r at low-frequency with increasing temperature indicates a larger contribution of thermally activated charges, such as space charges. Also, significant increase of $\tan\delta$ indicates the larger space charge polarization by carrier accumulation, attributing to the larger leakage current loss. For example, the value of $\tan\delta$ at 423K of each sample is over two times bigger than its original value at 298K.

Secondly, by comparing different films' $\tan\delta$ at low frequency range and same temperature range in Figure 16, it is clear that more Cr-doping leads to a greater $\tan\delta$ at certain

temperature. For example, the value of pure BFTO at 423K is much lower than any other film's value. This suggests that Cr-doping contributes to the space charge polarization by increasing the carrier concentration. And the value of $\text{BC}_{0.5}\text{F}_{0.5}\text{TO}$ at 423K is relatively lower than that of $\text{BC}_{0.3}\text{F}_{0.7}\text{TO}$, which can be still attributed to the suppression of the long-range carrier transport by plate-like grain shape.

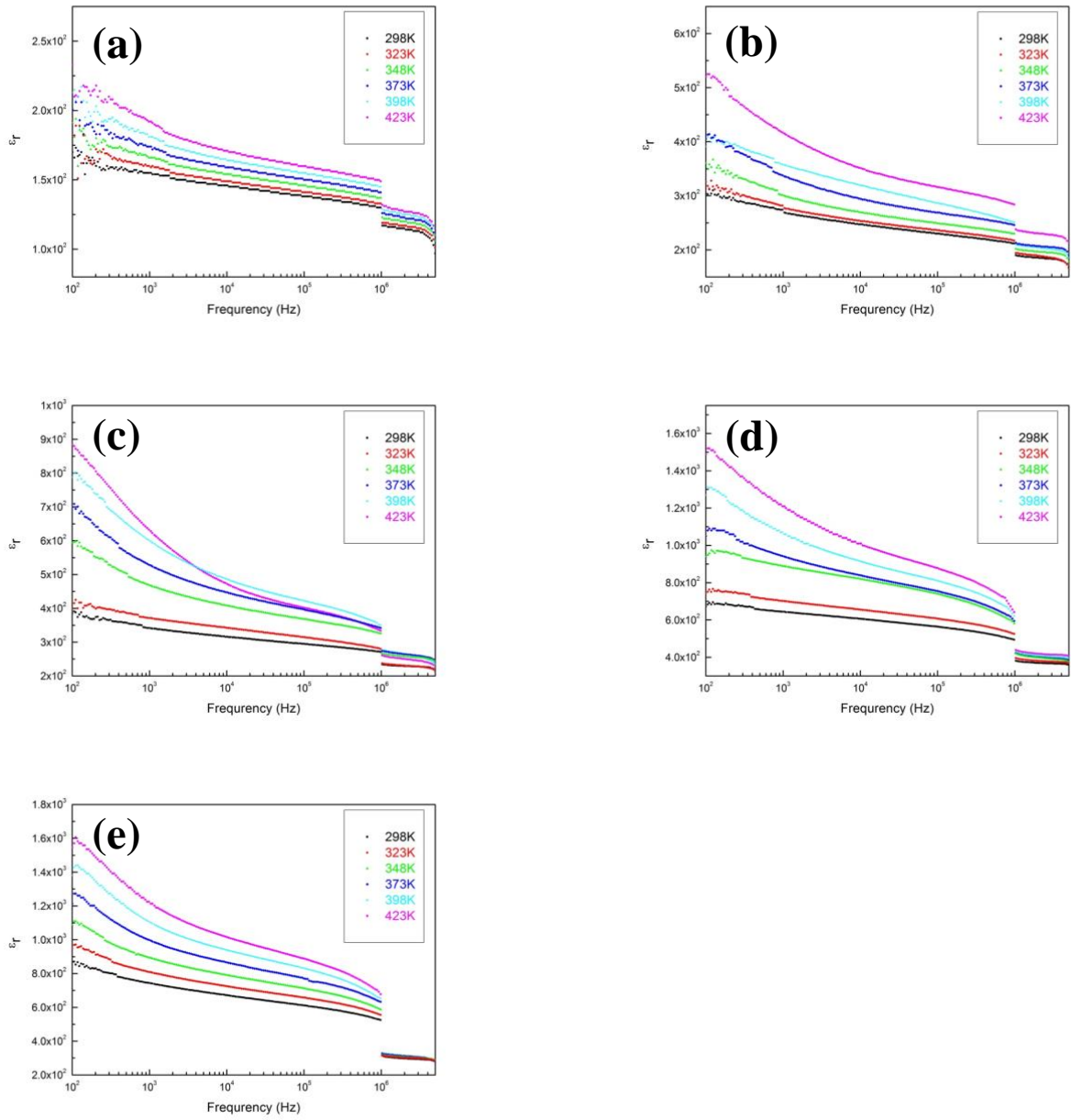


Figure 16. The Frequency Dependency of ϵ_r of the BCFTO Thin Films at Various Temperatures for: (a) $x=0$, (b) $x=0.1$, (c) $x=0.3$, (d) $x=0.5$, (e) $x=1$.

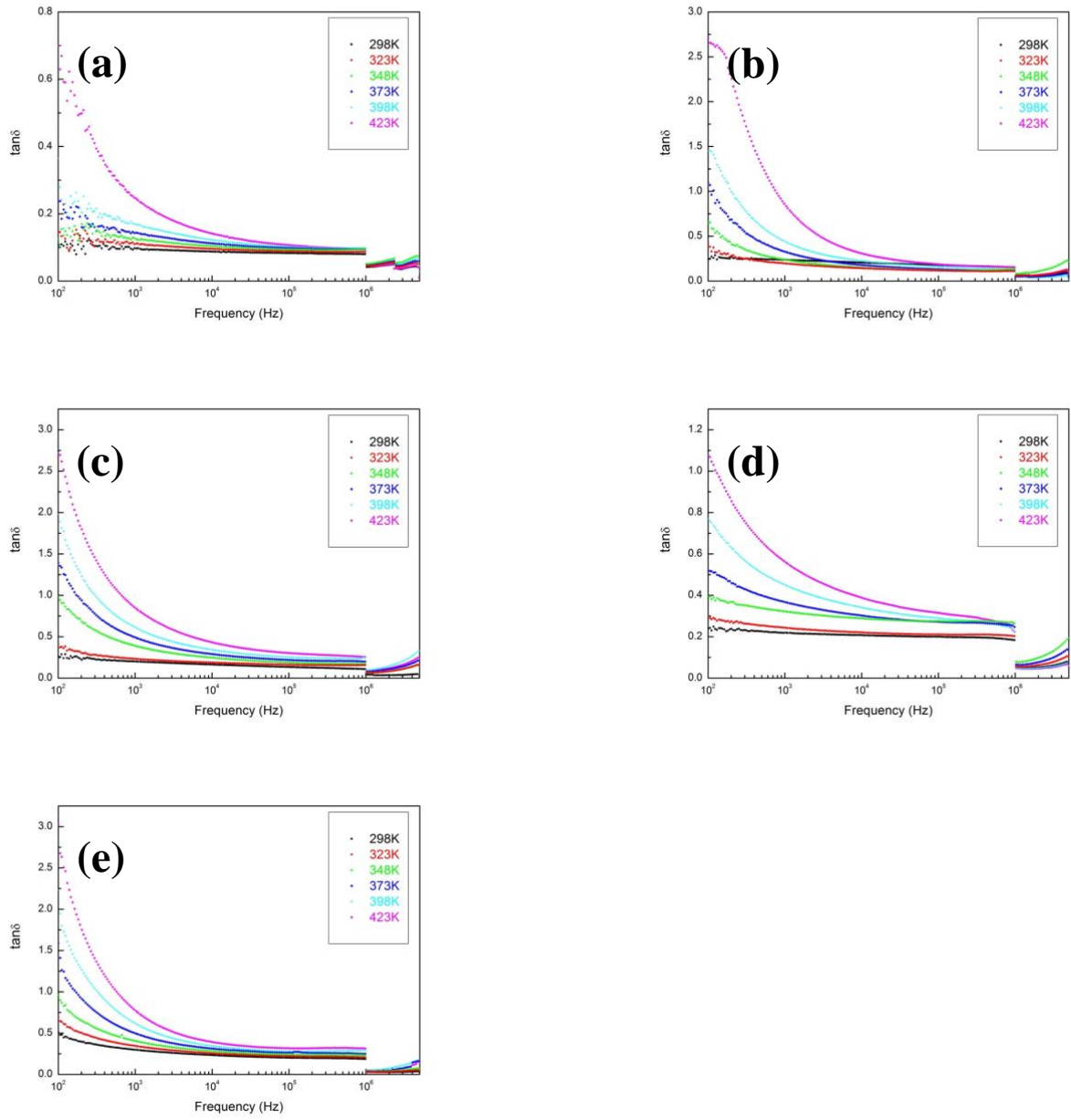


Figure 17. The Frequency Dependency of $\tan\delta$ of the BCFTO Thin Films at Various Temperatures for: (a) $x=0$, (b)

$x=0.1$, (c) $x=0.3$, (d) $x=0.5$, (e) $x=1$.

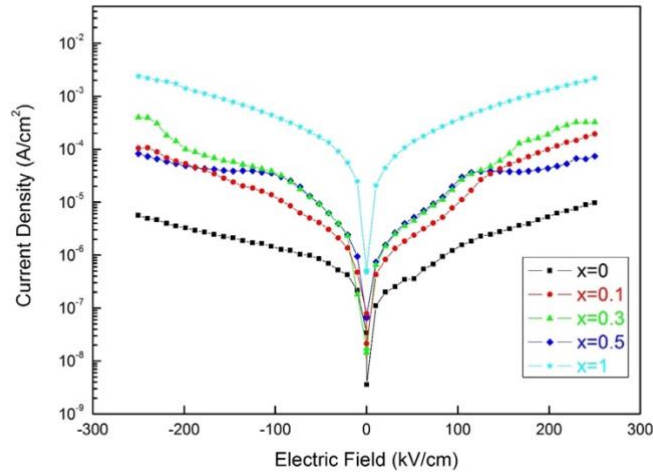


Figure 18. The Electric Field Dependence of Leakage Current Density (J-E) of All BCFTO Samples.

The typical leakage current density J at room temperature was measured for all samples annealed at 650°C and the results on a semi-log scale on the electric field with different Cr-doping content are shown in Figure 18. The DC voltage range was applied with a 0.4V step, ranged from -10V to 10V . A 20s soak time between each step was used to ensure the steady-state measurement.

Several features are noticeable. First, the leakage current density J value of pure BFTO displays at least one order of magnitude lower than those of other Cr-doped BCFTO films under the field over approximately 200 kV/cm . Second, the J value of the BCFTO gradually increased with the increasing of Cr-doping content. At an applied electric field of 200 kV/cm , the value of pure BCTO film is over 10^{-3} A/cm^2 , whereas it is about 10^{-5} A/cm^2 for the pure BFTO film. But, to the $\text{BC}_{0.5}\text{F}_{0.5}\text{TO}$ film, the J value didn't remain the rate of increasing compared with the

BC_{0.3}F_{0.7}TO films. Last but not least, it is noted that an increase in the leakage current is marginal in a range of $x=0.1-0.5$ (Y-axis of the graph is plotted in a log scale). This is consistent with our results and speculation on the relation between Cr doping, grain shape and carrier transport.

Impurity ion conductance, injected holes (or electrons) conductance and extrinsic defects carrier conductance are the main factors influencing the thin-film conductivity for metal–ferroelectrics–metal configuration at room temperature²⁶. In order to deeply understand the leakage behavior of the junction between the film and the electrode, several well-known mechanisms were studied by the various conduction mechanisms as shown in Figure 19. They are ohmic contact, bulk-limited Poole–Frenkel (PF) emission effect, interface-limited Fowler–Nordheim (FN) tunneling, interface-limited Schottky emission, and space-charge-limited current (SCLC)²⁵⁻²⁶. However, a part of samples ($x=0.1-0.5$) need to be remeasured in the future to better understand the leakage current mechanism because of their strange fluctuation.

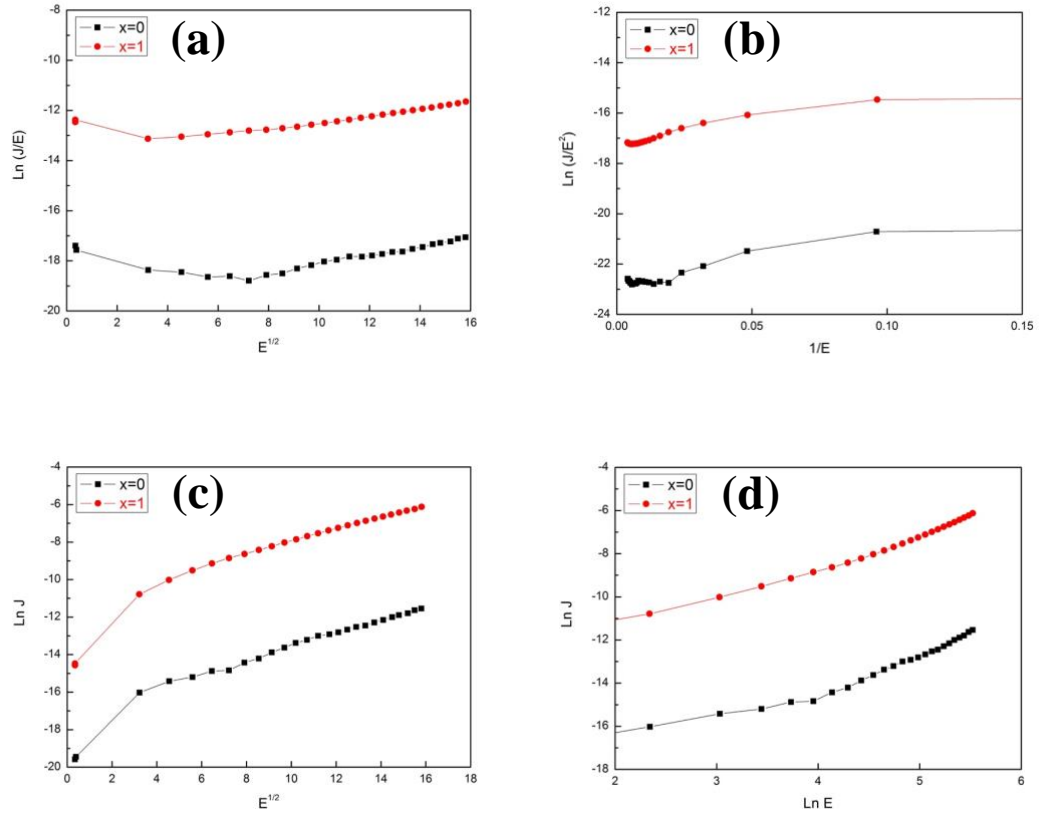


Figure 19. Various Fits of J-E Curves Using Different Leakage Current Mechanisms: (a) PF Emission: $\ln(J/E)$

Versus $E^{1/2}$ Curves, (b) FN Tunneling: $\ln(J/E^2)$ Versus $1/E$ Curves, (c) Schottky Emission: $\ln J$ Versus $E^{1/2}$ Curves,

(d) Ohmic and SCLC: $\ln J$ Versus $\ln E$ Curves.

If the leakage current is controlled by the bulk-limited PF emission effect, which originates from the field-assisted thermal ionization of trapped carriers into the conduction band of the semiconductors, then the leakage current density can be expressed in Equation 5-3:

$$J_{PF} = CE \exp\left[\frac{e(\sqrt{eE/\pi\epsilon_0\epsilon_{r0}} - E_t)}{kT}\right] \quad (5-3)$$

Where C and e are a constant and electronic charge, k and T are the Boltzmann constant and temperature in Kelvin, ϵ_0 and ϵ_{r0} are the dielectric constant of free space and optical dielectric constant of the film, and E_t is the trap ionization energy. The PF emission produces a linear relation between $\ln(J/E)$ and $E^{1/2}$ ²⁵⁻²⁶. However, no obvious linear relation to BFTO and BCTO were observed in this PF emission model with $\ln(J/E)$ verse $E^{1/2}$.

If the leakage current is controlled by the interface-limited FN tunneling, which may substantially contribute to the leakage current at high applied electric fields, then the leakage current density can be expressed in Equation 5-4:

$$J_{FN} = BE^2 \exp(C\phi_i^{3/2}/E) \quad (5-4)$$

Where B and C are the constants and ϕ_i is the potential barrier height. If the leakage current is dominated by the FN tunneling, there should be a linear relation between $\ln(J/E^2)$ and $1/E$ ²⁵⁻²⁶. However, no linear relation for BFTO and BCTO were observed in this FN tunneling model.

The interface-limited Schottky emission, which is based on the Schottky barrier at the interface of the metal electrode and the dielectric, can be expressed in Equation 5-5:

$$J_{SE} = AT^2 \exp\left(-\frac{\phi_b}{kT}\right) \exp\left(\frac{e\sqrt{eE/4\pi\epsilon_0\epsilon_{r0}}}{kT}\right) \quad (5-5)$$

Where A is the Richardson constant and ϕ_b is the Schottky barrier height. If the mechanism is controlled by the Schottky emission, a linear relation between $\ln J$ and $E^{1/2}$ should be observed²⁵⁻²⁶. However, no linear relations of BFTO and BCTO were observed in the Schottky emission model.

Finally, a power law relationship $\ln J$ and $\ln E$ is used to fit the curves in order to find out the mechanism, where s is the slope. Under low driving electric fields, all films are seemed to follow the ohmic contact mechanism with a slope value of $s \approx 1.26$, which is represented by the following Equation 5-6:

$$J_{ohmic} = e\mu N_e E \quad (5-6)$$

Where e is the electron charge, μ is the free carrier mobility, N_e is the density of the thermally stimulated electrons, and E is the applied electric field.

Under a high driving electric field, the charge injection from the electrodes into the ferroelectric film leads to the leakage current density starting to exhibit nonlinear behavior and the value of the slope gradually increase for all films ($s \approx 1 \sim 2$), implying a transition of the conduction mechanism from ohmic to SCLC²⁵⁻²⁶. The leakage current density for the SCLC mechanism is given by Equation 5-7:

$$J_{SCLC} = \left(\frac{9\mu\epsilon_0\epsilon_r\theta V^2}{8d^3} \right) \quad (5-7)$$

Where ϵ_0 and ϵ_r are the permittivity of free space and dielectric constant, respectively. V and d are the applied voltage and the thickness of the thin film, respectively. θ shows the ratio of the total density of free electrons to trapped electrons²⁵⁻²⁶. The SCLC mechanism implies that the leakage current migration doesn't depend on the carrier concentration but the mobility of carrier.

Table 1 The Conduction Mechanisms of BFTO and BCTO Films under Different Electric Field.

	x=0	x=1
Small electric field	Ohmic	Ohmic
Large electric field	SCLC	SCLC

Therefore, the conduction mechanisms of BFTO and BCTO thin films in our study can be roughly described as shown in Table 1. The mechanisms of them obey Ohmic contact law under a low electric field; under a high electric field, they roughly follow the space-charge-limited current (SCLC) model. SCLC mechanism confirms a role of the space charge in BCFTO. As electric field increases, the current density also increases, and more hole carriers are accumulated at the electrode-ferroelectric interface. This space charge controls the mobility of carriers under electric field. But further investigations for analyzing the conduction mechanisms of all BCFTO films are still needed.

6.0 Conclusion

Ferroelectric thin films $\text{Bi}_5\text{Cr}_x\text{Fe}_{1-x}\text{Ti}_3\text{O}_{15}$ (BCFTO) were successfully grown on Pt/Ti/SiO₂/Si/ substrates by chemical solution deposition. The effect of Cr-doping are characterized from the aspects of the crystal structure, bandgap, microstructure, ferroelectric/dielectric properties and electric transport.

In the range of $0 < x < 0.5$, the increase in Cr-doping content decreases the lattice distortion, changes the grain shape and increases carrier transport. This is attributed to the disordered distribution of Cr and Fe and the suppression of the oxygen vacancy formation.

At $x = 0.5$, the film has the smallest lattice distortion and the plate-like grain shape. This leads to the largest ferroelectric polarization, the smallest coercive field and the relatively small leakage current.

The conduction mechanisms of the BFTO and BCTO thin films are found to be electric-field dependent. Ohmic contact law and the space-charge-limited current (SCLC) model play an important role under a low electric field and high electric field, respectively.

Current results suggest that further research on the effect of annealing ambience to increase the oxygen vacancy is needed. A small increase in the oxygen vacancy by the thermal annealing in the reducing ambience may decrease the hole concentration and electric conductivity. If successful, this will result in insulating BCFTO ferroelectrics of high polarization and low coercive field.

Bibliography

1. Martin, L. W., & Rappe, A. M. (2016). Thin-film ferroelectric materials and their applications. *Nature Reviews Materials*, 2(2), 1-14.
2. Liu, J., Bai, W., Yang, J., Xu, W., Zhang, Y., Lin, T., ... & Chu, J. (2013). The Cr-substitution concentration dependence of the structural, electric and magnetic behaviors for Aurivillius $\text{Bi}_5\text{Ti}_3\text{FeO}_{15}$ multiferroic ceramics. *Journal of Applied Physics*, 114(23), 234101.
3. Bobić, J. D., Katiliute, R. M., Ivanov, M., Petrović, M. V., Ilić, N. I., Džunuzović, A. S., ... & Stojanović, B. D. (2016). Dielectric, ferroelectric and magnetic properties of La doped $\text{Bi}_5\text{Ti}_3\text{FeO}_{15}$ ceramics. *Journal of Materials Science: Materials in Electronics*, 27(3), 2448-2454.
4. Wang, Q., & Wang, C. M. (2020). Enhanced piezoelectric properties of Mn-modified $\text{Bi}_5\text{Ti}_3\text{FeO}_{15}$ for high-temperature applications. *Journal of the American Ceramic Society*, 103(4), 2686-2693.
5. Bai, Y., Chen, J., Wu, X., & Zhao, S. (2016). Photovoltaic behaviors regulated by band-gap and bipolar electrical cycling in holmium-doped $\text{Bi}_5\text{Ti}_3\text{FeO}_{15}$ ferroelectric films. *The Journal of Physical Chemistry C*, 120(43), 24637-24645.
6. Dias, J. A., Bretas, R. E. S., Marcondes, L. M. S., & Morelli, M. R. (2019). Optical and dielectric properties of Nd and Sm-doped $\text{Bi}_5\text{Ti}_3\text{FeO}_{15}$. *Journal of Materials Science: Materials in Electronics*, 30(18), 16812-16820.
7. Yuan, Y., Xiao, Z., Yang, B., & Huang, J. (2014). Arising applications of ferroelectric materials in photovoltaic devices. *Journal of Materials chemistry A*, 2(17), 6027-6041.
8. Bai, W., Chen, C., Yang, J., Zhang, Y., Qi, R., Huang, R., ... & Chu, J. (2015). Dielectric behaviors of Aurivillius $\text{Bi}_5\text{Ti}_3\text{Fe}_{0.5}\text{Cr}_{0.5}\text{O}_{15}$ multiferroic polycrystals: Determining the intrinsic magnetoelectric responses by impedance spectroscopy. *Scientific reports*, 5, 17846.
9. Moure, A. (2018). Review and perspectives of aurivillius structures as a lead-free piezoelectric system. *Applied Sciences*, 8(1), 62.
10. Fousek, J. (1991). Ferroelectricity: Remarks on historical aspects and present trends. *Ferroelectrics*, 113(1), 3-20.
11. Gonzalo, J. A., & Jiménez, B. (2008). *Ferroelectricity: The Fundamentals Collection*. John Wiley & Sons.
12. Sun, B., Wu, J., Gao, C., & Qian, M. (2007). Research on the torsional effect of piezoelectric quartz. *Sensors and Actuators A: Physical*, 136(1), 329-334.
13. Spaldin, N. A. (2010). *Magnetic materials: fundamentals and applications*. Cambridge university press.
14. Damjanovic, D. (1998). Ferroelectric, dielectric and piezoelectric properties of ferroelectric thin films and ceramics. *Reports on Progress in Physics*, 61(9), 1267.

15. Fousek, J. (1994, August). Joseph valasek and the discovery of ferroelectricity. In Proceedings of 1994 IEEE International Symposium on Applications of Ferroelectrics (pp. 1-5). IEEE.
16. Busch, G. (1987). Early history of ferroelectricity. *Ferroelectrics*, 74(1), 267-284.
17. Busch, G. (1987). How I discovered the ferroelectric properties of KH_2PO_4 . *Ferroelectrics*, 71(1), 43-47.
18. Kanzig, W. (1987). History of ferroelectricity 1938-1955. *Ferroelectrics*, 74(1), 285-291.
19. Scott, J. F., & De Araujo, C. A. P. (1989). Ferroelectric memories. *Science*, 246(4936), 1400-1405.
20. Ramesh, R. (Ed.). (2013). *Thin film ferroelectric materials and devices (Vol. 3)*. Springer Science & Business Media.
21. Stojanovic, B. (2018). *Magnetic, Ferroelectric, and Multiferroic Metal Oxides*. Elsevier.
22. Liu, G., Zhang, S., Jiang, W., & Cao, W. (2015). Losses in ferroelectric materials. *Materials Science and Engineering: R: Reports*, 89, 1-48.
23. Song, D. P., Yang, J., Yang, B. B., Wang, Y., Chen, L. Y., Wang, F., & Zhu, X. B. (2019). Energy storage in $\text{BaBi}_4\text{Ti}_4\text{O}_{15}$ thin films with high efficiency. *Journal of Applied Physics*, 125(13), 134101.
24. Huang, H., & Scott, J. F. (Eds.). (2019). *Ferroelectric materials for energy applications*. Retrieved from <https://ebookcentral.proquest.com>
25. Wang, W., Sun, J. B., Mao, X. Y., & Chen, X. B. (2008). Structural and electrical characterization of chemical-solution-derived $\text{Bi}_5\text{FeTi}_3\text{O}_{15}$ thin films. *Journal of Physics D: Applied Physics*, 41(15), 155418.
26. Song, D., Yang, J., Yang, B., Chen, L., Wang, F., & Zhu, X. (2018). Evolution of structure and ferroelectricity in Aurivillius $\text{Bi}_4\text{Bi}_{n-3}\text{Fe}_{n-3}\text{Ti}_3\text{O}_{3n+3}$ thin films. *Journal of Materials Chemistry C*, 6(32), 8618-8627.
27. Rabe, K. M., Dawber, M., Lichtensteiger, C., Ahn, C. H., & Triscone, J. M. (2007). Modern physics of ferroelectrics: Essential background. In *Physics of Ferroelectrics* (pp. 1-30). Springer, Berlin, Heidelberg.
28. Long, C., Fan, H., Li, M., Dong, G., & Li, Q. (2014). Crystal structure and enhanced electromechanical properties of Aurivillius ferroelectric ceramics, $\text{Bi}_4\text{Ti}_{3-x}(\text{Mg}_{1/3}\text{Nb}_{2/3})_x\text{O}_{12}$. *Scripta Materialia*, 75, 70-73.
29. Goto, T., Noguchi, Y., Soga, M., & Miyayama, M. (2005). Effects of Nd substitution on the polarization properties and electronic structures of bismuth titanate single crystals. *Materials research bulletin*, 40(6), 1044-1051.
30. Shimakawa, Y., Kubo, Y., Tauchi, Y., Asano, H., Kamiyama, T., Izumi, F., & Hiroi, Z. (2001). Crystal and electronic structures of $\text{Bi}_{4-x}\text{La}_x\text{Ti}_3\text{O}_{12}$ ferroelectric materials. *Applied Physics Letters*, 79(17), 2791-2793.

31. Qi, J., Zhang, Y., Wang, Y., Liu, Y., Wei, M., Zhang, J., ... & Yang, J. (2017). Effect of Cr doping on the phase structure, surface appearance and magnetic property of BiFeO₃ thin films prepared via sol-gel technology. *Journal of Materials Science: Materials in Electronics*, 28(23), 17490-17498.
32. Lee, S. U., Kim, S. S., Jo, H. K., Park, M. H., Kim, J. W., & Bhalla, A. S. (2007). Electrical properties of Cr-doped BiFeO₃ thin films fabricated on the p-type Si (100) substrate by chemical solution deposition. *Journal of Applied Physics*, 102(4), 044107.
33. Kim, J. K., Kim, S. S., Kim, W. J., Bhalla, A. S., & Guo, R. (2006). Enhanced ferroelectric properties of Cr-doped BiFeO₃ thin films grown by chemical solution deposition. *Applied physics letters*, 88(13), 132901.
34. Nie, C., Chen, J., Bai, Y., & Zhao, S. (2016). The ferroelectric photovoltaic spectral response regulated by band-gap in BiFe_{0.9}Cr_{0.1}O₃ films. *Materials Letters*, 175, 258-261.
35. Kooriyattil, S., Katiyar, R. K., Pavunny, S. P., Morell, G., & Katiyar, R. S. (2014). Photovoltaic properties of Aurivillius phase Bi₅FeTi₃O₁₅ thin films grown by pulsed laser deposition. *Applied Physics Letters*, 105(7), 072908.
36. Seidel, J., Fu, D., Yang, S. Y., Alarcón-Lladó, E., Wu, J., Ramesh, R., & Ager III, J. W. (2011). Efficient photovoltaic current generation at ferroelectric domain walls. *Physical review letters*, 107(12), 126805.
37. Li, J. B., Rao, G. H., Liang, J. K., Liu, Y. H., Luo, J., & Chen, J. R. (2007). Magnetic properties of Bi(Fe_{1-x}Cr_x) O₃ synthesized by a combustion method. *Applied physics letters*, 90(16), 162513.
38. Oumezzine, M., Peña, O., Kallel, S., Guizouarn, T., & Oumezzine, M. (2012). Structural studies and magnetic and transport properties of Cr-substituted La_{0.67}Ba_{0.33}Mn_{1-x}Cr_xO₃ (0 ≤ x ≤ 0.15) perovskites. *Journal of alloys and compounds*, 533, 33-40.
39. Mohamed, M. B., Wang, H., & Fuess, H. (2010). Dielectric relaxation and magnetic properties of Cr doped GaFeO₃. *Journal of Physics D: Applied Physics*, 43(45), 455409.
40. Biswas, S., Khan, M. H., Pal, S., & Bose, E. (2013). Evolution of magnetic properties in Cr doped manganites Gd_{0.7}Ca_{0.3}Mn_{1-x}Cr_xO₃ (x=0-0.5). *Journal of magnetism and magnetic materials*, 328, 31-34.
41. Bai, W., Gao, Y. Q., Zhu, J. Y., Meng, X. J., Lin, T., Yang, J., ... & Chu, J. H. (2011). Electrical, magnetic, and optical properties in multiferroic Bi₅Ti₃FeO₁₅ thin films prepared by a chemical solution deposition route. *Journal of Applied Physics*, 109(6), 064901.
42. Dong, X. W., Wang, K. F., Wan, J. G., Zhu, J. S., & Liu, J. M. (2008). Magnetocapacitance of polycrystalline Bi₅Ti₃FeO₁₅ prepared by sol-gel method. *Journal of Applied Physics*, 103(9), 094101.
43. Mao, X. Y., Wang, W., & Chen, X. B. (2008). Electrical and magnetic properties of Bi₅FeTi₃O₁₅ compound prepared by inserting BiFeO₃ into Bi₄Ti₃O₁₂. *Solid state communications*, 147(5-6), 186-189.

44. Mao, X., Sun, H., Wang, W., Lu, Y., & Chen, X. (2012). Effects of Co-substitutes on multiferroic properties of $\text{Bi}_5\text{FeTi}_3\text{O}_{15}$ ceramics. *Solid state communications*, 152(6), 483-487.
45. Singh, R. S., Bhimasankaram, T., Kumar, G. S., & Suryanarayana, S. V. (1994). Dielectric and magnetoelectric properties of $\text{Bi}_5\text{FeTi}_3\text{O}_{15}$. *Solid state communications*, 91(7), 567-569.
46. Zhang, S. T., Chen, Y. F., Liu, Z. G., Ming, N. B., Wang, J., & Cheng, G. X. (2005). Structures and electrical properties of $\text{Bi}_5\text{FeTi}_3\text{O}_{15}$ thin films. *Journal of applied physics*, 97(10), 104106.
47. Jonscher, A. K. (1999). Dielectric relaxation in solids. *Journal of Physics D: Applied Physics*, 32(14), R57.
48. Bai, W., Chen, G., Zhu, J. Y., Yang, J., Lin, T., Meng, X. J., ... & Chu, J. H. (2012). Dielectric responses and scaling behaviors in Aurivillius $\text{Bi}_6\text{Ti}_3\text{Fe}_2\text{O}_{18}$ multiferroic thin films. *Applied Physics Letters*, 100(8), 082902.